COMMUNICATIONS PHYSICS

ARTICLE

https://doi.org/10.1038/s42005-019-0243-4 OPEN

Unveiling the vortex glass phase in the surface and volume of a type-II superconductor

Jazmín Aragón Sánchez[1], Raúl Cortés Maldonado[1], Néstor R. Cejas Bolecek[1], Gonzalo Rumi[1], Pablo Pedrazzini[1], Moira I. Dolz[2], Gladys Nieva[1], Cornelis J. van der Beek[3], Marcin Konczykowski[4], Charles D. Dewhurst[5], Robert Cubitt[5], Alejandro B. Kolton[1], Alain Pautrat[6] & Yanina Fasano[1*]

Order-disorder transitions between glassy phases are common in nature and yet a comprehensive survey on the entailed structural changes is challenging since the constituents are in the micro-scale. Vortex matter in type-II superconductors is a model system where some of these experimental challenges can be tackled. Samples with point disorder present a glassy transition on increasing the density of vortices. A glassy yet quasi-crystalline phase, the Bragg glass, nucleates at low densities. The vortex glass stable at high densities is expected to be disordered, however its detailed structural properties remained experimentally elusive. Here we show that the vortex glass has large crystallites with in-plane positional displacements growing algebraically and short-range orientational order. Furthermore, the vortex glass has a finite and almost constant correlation length along the direction of vortices, in sharp contrast with strong entanglement. These results are important for the understanding of disorder-driven phase transitions in glassy condensed matter.

[1] Centro Atómico Bariloche and Instituto Balseiro, CNEA, Universidad Nacional de Cuyo, CONICET, 8400 Bariloche, Argentina. [2] Universidad Nacional de San Luis and Instituto de Física Aplicada, CONICET, 5700 San Luis, Argentina. [3] Centre de Nanosciences et de Nanotechnologies, CNRS, Université Paris-Sud, Université Paris-Saclay, 91120 Palaiseau, France. [4] Laboratoire des Solides Irradiés, École Polytechnique, CNRS, 91128 Palaiseau, France. [5] Institut Laue-Langevin, B.P. 156, 38042 Grenoble Cedex 9, France. [6] Laboratoire CRISMAT-EnsiCaen, Caen, France. *email: yanina.fasano@cab.cnea.gov.ar

Order–disorder structural transitions are so ubiquitous in nature that we are faced to solid-to-liquid and solid-to-solid structural transformations in everyday experience. Quite frequently, the unavoidable disorder present in the materials favors the stabilization of glassy phases, such as spin, electric, and superconducting glass systems[1]. In order to expand the potential applications of these materials, direct access to the microscopic structural changes entailed at order–disorder transformations is mandatory. Considerable data is available in the solid-to-liquid case, concerning monolayers of electrons trapped on the surface of liquid He[2], colloidal and hard spheres[3–5], plasma crystals[6], and superparamagnetic colloidal particles[7]. These experiments support a dislocation-mediated two-stage melting with an intermediate hexatic phase in the case of melting in two dimensions[8–12], spin[8], and superfluid transitions[13]. Only a handful of studies have directly probed the structural changes entailed in glass-to-glass order–disorder transitions in three dimensions.

Vortex matter in type-II superconductors is a model condensed matter system to study this problem since the energy scales and dimensionality can be easily tuned by control parameters. The energy scales governing the occurrence of order–disorder transformations are vortex–vortex repulsion, vortex-pinning interaction, and thermal fluctuations, respectively, controlled by magnetic field H, sample disorder, and temperature. Order–disorder transitions in vortex matter occur since the vortex–vortex interaction tends to form a triangular lattice whereas thermal fluctuations and the pinning produced by the sample disorder conspire against the stabilization of a perfect crystal[14]. Some experimental works image the structural changes entailed in glass-to-glass transitions in vortex matter at the sample surface[15–23], but since they study small fields-of-view do not provide information on the evolution of correlation functions at long distances. Regarding the longitudinal direction, some studies in extremely layered cuprates found that at the melting[24] and glass-to-glass[25] transitions the superconducting phase coherence abruptly jumps down. Since vortex lines in these materials result from the piling up of pancake vortices located in the CuO planes, this jump in phase coherence was interpreted as an indication of enhanced vortex wandering. However, the superconducting phase coherence is only sensitive to the misalignment of pancake vortices at very short lengthscales ($\sim$ 15 Å), and thus inferring information about the longitudinal structural properties of vortex matter is not straightforward from such measurements. Therefore, a comprehensive description of the problem requires imaging the in-plane as well as out-of-plane structural changes taking place in order–disorder transitions. Experimentally, this is quite challenging since it requires the ability to image, with single-particle resolution, vortex matter at the surface and bulk of the sample. This is the problem we are addressing here.

In some superconducting glasses, as those nucleated in extremely layered high-T_c's, a quasi-crystalline state of matter is stable at low vortex densities: the Bragg glass phase presenting a weak logarithmic decay of positional order and glassy dynamics[26–28]. On increasing vortex density (magnetic field), a first-order transition takes place at a characteristic order–disorder transition field $B_{ord-dis}$[29]. The vortex glass phase stable at $B > B_{ord-dis}$ is expected to present non-divergent peaks in the structure factor unlike the Bragg glass. For the $Bi_2Sr_2CaCu_2O_{8+\delta}$ superconductor we study here, $B_{ord-dis}$ is concomitant to the second-peak effect[30–33], associated to a peak in the superconductor critical current when increasing field or temperature. This is due to pinning energy overcoming elastic energy in the disordered phase. The $B_{ord-dis}$ field at which the vortex density presents a jump[30] coincides with the onset field of the second-peak effect, B_{ON}. At high temperatures, the order–disorder transition continues as a first-order melting at the B_{FOT} line separating the Bragg glass from the vortex liquid [34].

The degree of disorder of the vortex glass raised discrepancy in the literature since theoretical works propose different scenarios, and conclusive experimental evidence was not yet available. Theoretical works suggest it presents either a hexatic nature with exponentially decaying positional order in the plane[35], or a proliferation of in-plane defects with entanglement along the sample thickness[31,36,37]. These latter expectations were put in context with data showing that the superconducting phase difference jumps down both at $B_{ord-dis}$ and B_{FOT}[25]. Nevertheless, since the phase difference remains finite and is sensitive to vortex roughening at short distances, these results cannot be considered as an evidence of the vortex glass being either a completely decoupled or a highly entangled structure. This point is important for the interpretation of our data combining the quantitative characterization of the in-plane and longitudinal structural properties of the vortex glass.

We perform this study by means of small-angle neutron scattering (SANS) experiments, a bulk-sensitive reciprocal-space technique that allows to extract quantitative information on real-space correlation lengths. For the superconducting glass we study here, previous SANS data reveal that the vortex diffraction pattern does not significantly change on traversing $B_{ord-dis}$, but the scattered intensity is strongly reduced for $B > B_{ord-dis}$[38,39]. Therefore, precise details on the structural properties of the vortex glass phase were not accessible in those works. A similar resolution-limited problem was also reported for SANS data in the vortex glass phase of other superconductors[28,40]. Therefore, SANS experiments with improved resolution are needed to characterize the fine structural changes entailed at the glass-to-glass transformation. In addition, in this work we combine SANS measurements with direct imaging of the $Bi_2Sr_2CaCu_2O_{8+\delta}$ vortex structure in large fields-of-view at the surface of the sample. On traversing the Bragg-to-vortex glass transition, we unveil the evolution of the in-plane and longitudinal vortex correlation lengths, and the distance-evolution of the in-plane orientational and positional correlation functions. Our results shed light on the impact of disorder in glass-to-glass transitions in soft condensed matter systems composed of elastic lines, signposting that entanglement in the longitudinal direction is not mandatory in transformations with proliferation of topological defects.

Results

Point disorder effect on the Bragg-to-vortex glass transition. In pristine $Bi_2Sr_2CaCu_2O_{8+\delta}$ vortex matter, $B_{ord-dis} \sim 200 - 300$ Gauss, well above the vortex density range probed by most real-space techniques that grant access to wide fields-of-view of thousands of vortices[41]. However, introducing extra point disorder in the samples by irradiation with electrons results in a significant lowering of the order–disorder line[32,42]. This allows us to apply the magnetic decoration technique (MD)[43] to image, over large fields-of-view, the structural changes taking place at the surface of these samples on traversing $B_{ord-dis}$.

Our samples are pristine (P) and electron-irradiated $Bi_2Sr_2CaCu_2O_{8+\delta}$ single crystals. Samples P include a millimetric-large single crystal for SANS, and 30 single crystals from different sample growers for MD, one of them a small part of the large crystal (see Methods). MD data as a function of field are similar for all the P single crystals studied. We also study two electron-irradiated samples, A and B, irradiated with 2.3 MeV electrons at 20 K. During irradiation, electrons traverse the sample thickness generating a random distribution of atomic point defects: $\sim$ 10% of atoms, depending on the irradiation dose, may be displaced

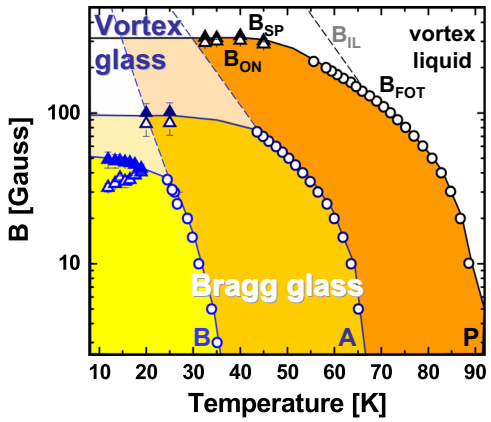

Fig. 1 Vortex phase diagram for pristine (P) and electron-irradiated (A and B) $Bi_2Sr_2CaCu_2O_{8+\delta}$ samples from local dc and ac Hall magnetometry measurements. Sample A was irradiated with 1.7×10^{19} e/cm^2 and sample B with 7.4×10^{19} e/cm^2. First-order transition lines B_{FOT} (open circles) and $B_{ord-dis} = B_{ON}$ (open triangles) separate the Bragg glass from the vortex liquid phase at high temperatures, and the vortex glass at high fields. Full triangles signpost the location of the so-called second peak in the critical current B_{SP}. Dashed lines represent the irreversibility line B_{IL}, located very close to B_{FOT} for the fields at which the Bragg glass is stable. Solid lines are guides to the eye; error bars are the standard error of the mean

from their initial position. This produces a decrease of $B_{ord-dis}$[32] that we track by applying dc and ac local Hall magnetometry. Detailed data on the detection of B_{FOT} and $B_{ord-dis} = B_{ON}$ can be found in Supplementary Note 1.

Figure 1 shows the vortex phase diagram for pristine and electron-irradiated $Bi_2Sr_2CaCu_2O_{8+\delta}$ samples. Increasing the dose of electron-irradiation produces a systematic decrease of T_c and $B_{ord-dis}$[42], and then the Bragg glass spans a smaller $B-T$ phase region. At low temperatures, sample A has a $B_{ord-dis} = 85(-5)$ Gauss and for sample B this value is even reduced to $\sim 40(-8)$ Gauss. This transition field also depends on the oxygen-doping and annealing of the samples[32,44], and for this reason sample B presents the smallest reported value of $B_{ord-dis}$ obtained by electron irradiation. This allowed us to reveal the structural properties of the vortex glass phase in extended fields-of-view by means of MD.

Bragg-to-vortex glass transformation from real-space imaging. Figure 2 shows MD snapshots with more than 1500 individually resolved vortices (black dots) taken after field-cooling the samples down to 4.2 K, at different applied fields. Changing field varies the lattice spacing of the hexagonal vortex lattice $a_0 = 1.075\sqrt{\Phi_0/B}$. Vortices are decorated with Fe particles attracted by the local field gradient generated around the cores. The decorated structures were frozen, at length scales of a_0, at temperatures at which the pinning generated by disorder sets in refs. [43,45]. This freezing temperature is some Kelvin below the temperature at which magnetic response becomes irreversible[46], see B_{IL} lines in Fig. 1. For $B \le B_{ord-dis}$ the B_{IL} line coincides with the melting line B_{FOT}.

Panels (a) and (b) of Fig. 2 are snapshots of vortex positions taken at $B < B_{ord-dis}$ in the Bragg glass phase: the structure is single-crystalline and presents very few topological defects associated with non-sixfold coordinated vortices for $B > 15$ Gauss. For smaller fields the structure breaks into small crystallites for pristine[47] as well as electron-irradiated samples. This polycrystals result from vortex–vortex interaction weakening and disorder becoming more relevant on the viscous freezing dynamics [47].

Vortices are better resolved by MD in pristine than in electron-irradiated samples, in agreement with the enhancement of the penetration depth $\lambda(0)$ when irradiating with electrons[42]. For samples A and B, from the difference in the entropy-jump at B_{FOT}[42], we estimate $\lambda(0)$ is 30% larger than in P samples. If $\lambda(0)$ increases, the local field gradient decreases and the magnetic force attracting Fe particles towards vortices diminishes. Then the field up to which individual vortices can be resolved with MD in electron-irradiated samples is reduced to ~ 90 Gauss.

Nevertheless, for sample B this field is high enough as to take snapshots of the vortex glass in extended fields-of-view. Figure 2 shows the largest picture of the vortex glass phase obtained for $B/B_{ord-dis} = 1.62$, with more than 1500 vortices. The over-imposed Delaunay triangulation joining first-neighbor vortices highlights the presence of grain boundaries separating large crystallites with hundreds of vortices. The misalignment of crystallites varies between 20° and 30°. Roughly 6% of vortices are non-sixfold coordinated and belong to different defects: 60% are in grain boundaries (violet triangles), 19% are in isolated edge dislocations (orange triangles), and the remaining 21% are in twisted-bond deformations (pink triangles). Isolated edge dislocations are plastic deformations entailing the nucleation of two extra vortex planes; twisted bonds are local elastic deformations made of two adjacent edge dislocations with opposite Burgers vectors and no extra plane of vortices. This snapshot of the vortex glass reveals that, within a crystallite, isolated edge dislocations entail plastic deformations even at large length scales. Indeed, only $\sim 40\%$ of the observed edge dislocations are paired with their Burgers vectors pointing in opposite directions (red arrows in Fig. 2c).

The proliferation of topological defects in the vortex glass phase contrasts with most of the Bragg glass phase being single-crystalline with a fraction of non-sixfold coordinated vortices $\rho_{def} < 1\%$, see Fig. 3a for data in samples A, B and P. As mentioned, at low fields $B/B_{ord-dis} \lesssim 0.01$ the structure fractures into small crystallites and then $\rho_{def} \sim 50\%$. However, on increasing field the structure is single crystalline and ρ_{def} decays dramatically and stagnates below 1% for $B/B_{ord-dis} \gtrsim 0.1$. This phenomenology is common to P and electron-irradiated samples, but the precise $B/B_{ord-dis}$ value at which the structure becomes single-crystalline depends on the magnitude of point disorder. Figure 3b shows the patterns resulting from calculating the structure factor from the individual vortex positions detected at the sample surface, namely $S_{MD}(q,\Psi) = |\tilde{\rho}(q_x,q_y)|^2_{z=0}$, with $\tilde{\rho}$ the Fourier transform of the density of vortex lines $\rho(x,y,z) = \frac{1}{t}\Sigma_{j=1}^{N}\delta(x-x_j(z))\delta(y-y_j(z))$ with t the thickness of the sample and N the number of vortices. Well within the vortex glass, ρ_{def} enhances up to 6.5% at $B/B_{ord-dis} = 1.62$ and in our experimental field-of-view the structure presents four large crystallites, resulting in multiple Bragg peaks in the $S_{MD}(q,\Psi)$ pattern.

Fracturing into large non-hexatic domains in the vortex glass. Theoretical studies for order–disorder transitions in two dimensions predict, between the ordered crystal and the liquid, an intermediate hexatic phase with long-range orientational and short-range positional orders[8]. Whether this is a scenario that also holds for three-dimensional systems will provide useful information for describing order–disorder transitions on general grounds. A seminal work for the intermediate dimensionality case of thick superconducting films reported a first-order transition to a high-field vortex state with strongly reduced longitudinal correlations, at odds with hexatic order [48].

Figure 4a, b show the evolution of the orientational order at the surface of the vortex structure on crossing $B_{ord-dis}$. We

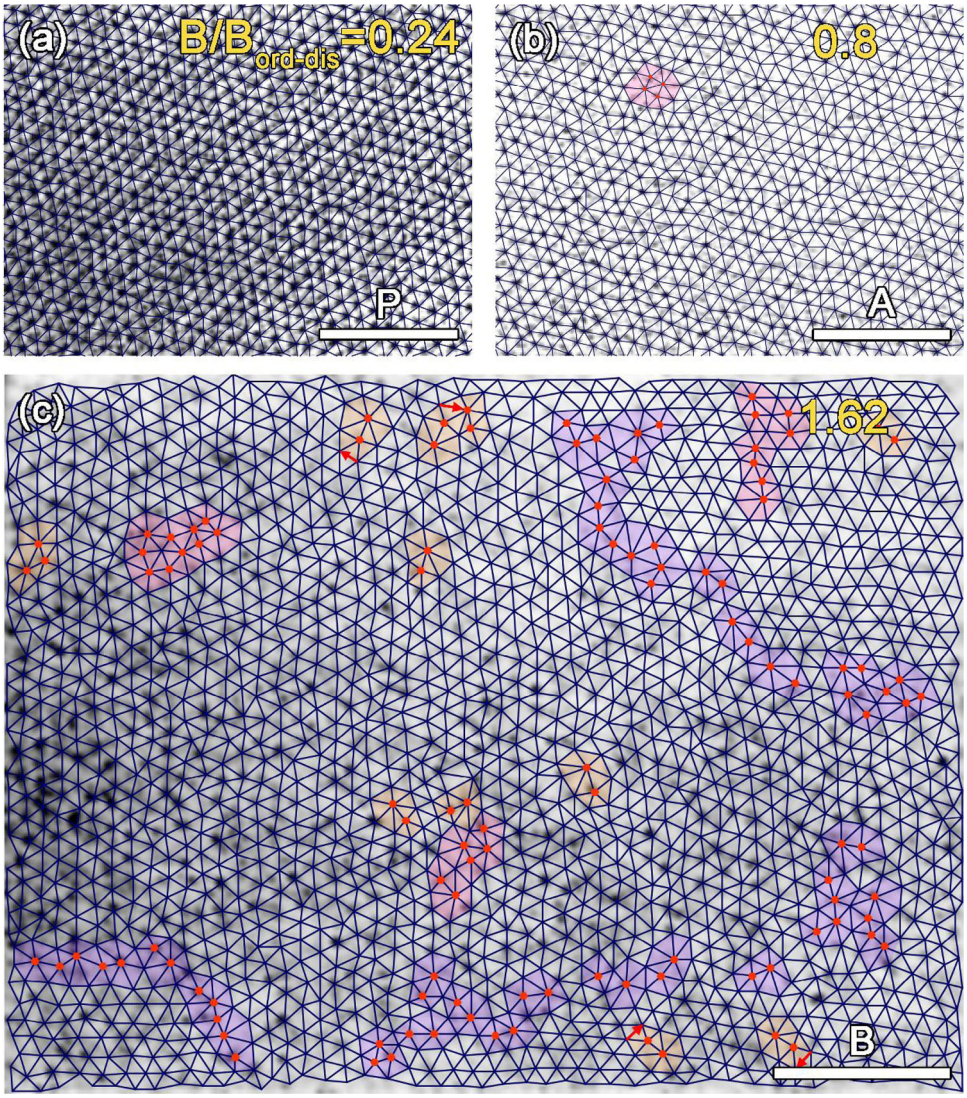

Fig. 2 Magnetic decoration images of individual vortices (black dots) in the Bragg and the vortex glass phases of pristine (P) and electron-irradiated (A and B) $Bi_2Sr_2CaCu_2O_{8+\delta}$ samples. Images are taken with an scanning-electron microscope at room temperature after performing the magnetic decoration experiments. Vortex structures in the Bragg glass phase for **a** $B/B_{\mathrm{ord-dis}} = 0.28$ in sample P and **b** $B/B_{\mathrm{ord-dis}} = 0.8$ in sample A. **c** Large field-of-view snapshot of the vortex-glass phase observed in sample B for $B/B_{\mathrm{ord-dis}} = 1.62$. Delaunay triangulations are superimposed on the structures: neighboring vortices are connected by dark blue lines and non-sixfold coordinated vortices are highlighted in red. Topological defects indicated with colors: grain boundaries highlighted in violet, edge dislocations in orange and twisted bonds in pink. Red arrows indicate the Burgers vectors of paired edge dislocations; no arrows are shown if dislocations seem to be unpaired in our experimental field-of-view. White bars indicate 5 μm

characterize the orientational order with the correlation function $G_6(r) = \langle \Psi_6(0)\Psi_6^*(r)\rangle$ measuring the distance-evolution of the hexagonal orientational order parameter $\Psi_6(\mathbf{r} = \mathbf{r_i}) = \Sigma_{j=1}^{n}(1/n)\exp(6i\theta_{ij})$ calculated from the bond angles of nearest neighbor vortices i and j, θ_{ij}. For $B/B_{\mathrm{ord-dis}} \leq 0.1$, $G_6(r)$ starts decaying algebraically up to a characteristic length of the size of the crystallites (see arrows) whereas for larger distances decays exponentially. On increasing field within the Bragg glass ($0.1 < B/B_{\mathrm{ord-dis}} < 1$), single-crystalline vortex structures are observed and coincidentally G_6 decays algebraically at all distances. The field-evolution of the exponent η of this algebraic decay is shown in Fig. 4c: it decreases dramatically when passing from the polycrystalline to the single-crystalline structures and remains almost constant for $B/B_{\mathrm{ord-dis}} > 0.2$. This stagnation is expected for a phase presenting long-range orientational order such as the Bragg glass. Interestingly, the saturation value $\eta \sim 0.025$ found at the surface of the Bragg glass is one order of magnitude smaller than that found in single-crystalline vanadium from SANS measurements[23]. This indicates that vortex meandering within the sample thickness is significant, even though the orientational order of the Bragg glass is long-ranged in the whole sample volume.

The vortex glass phase presents a faster decay of orientational order: even within the larger crystallite of the center of Fig. 2c, G_6 decays exponentially with distance. Once the limits of the grain boundary are reached, there is a kink in G_6 and the decay continues to be exponential. Therefore, the orientational order of the vortex glass at the surface of $Bi_2Sr_2CaCu_2O_{8+\delta}$ samples is at odds with theories of the vortex glass being a hexatic phase (with algebraically decaying G_6)[35], but is evocative of another proposal of a multi-domain glassy phase separating the Bragg glass and the vortex liquid[49]. The fracturing of the vortex glass into large domains could be a non-equilibrium feature, due to finite cooling rates in field-cooling experiments[40]. Nevertheless, the vortex glass presents non-hexatic order already inside the crystallites.

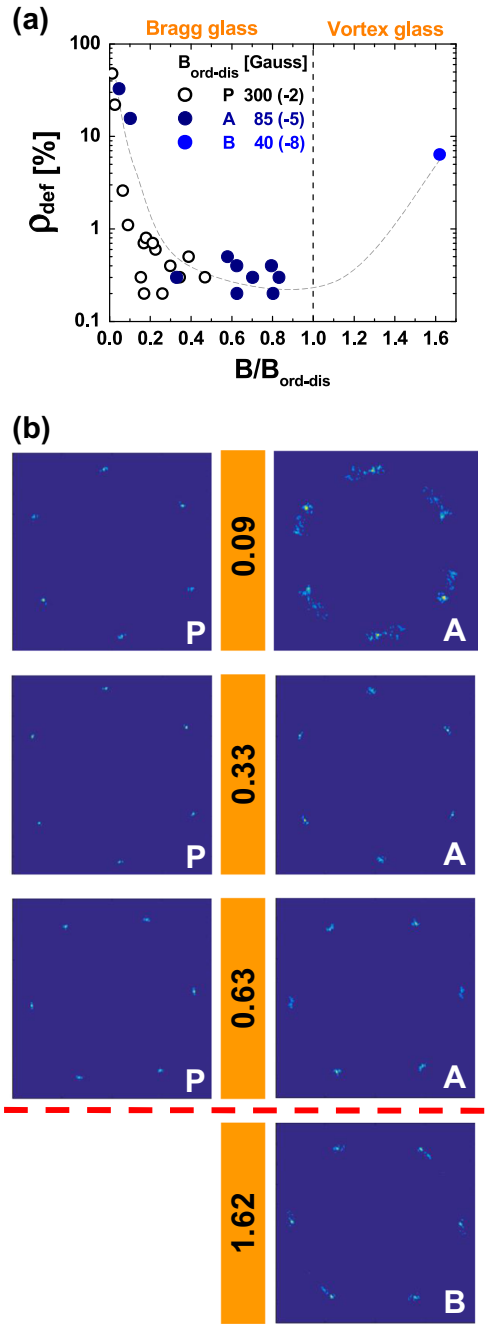

Fig. 3 Topological defects and structure factor data for the Bragg and vortex glass phases of $Bi_2Sr_2CaCu_2O_{8+\delta}$ vortex matter at the surface of the samples. **a** Fraction of non-sixfold coordinated vortices, ρ_{def}, as a function of the magnetic field normalized by the order-disorder transition field, $B/B_{ord-dis}$. The standard error of the mean is within the size of the points. **b** Structure factor $S_{MD}(q,\Psi)$ of the vortex structure observed by magnetically decorating the individual vortex positions in pristine P and electron-irradiated A and B samples

SANS data probing the structural properties of the vortex glass in the whole thickness of the sample are consistent with this degradation of orientational order at the surface. The intensity measured in a SANS experiment[39] is equal to the structure factor times the magnetic form factor $f(q)$, averaged over the entire volume of the sample, $I(q) = S_{SANS}(q,\Psi) \cdot f^2(q)$. The structure factor measured in SANS collects information on the meandering of vortices along the sample thickness, namely $S_{SANS}(q,\Psi) = |\int \rho(q_x,q_y,z)dz|^2$. Figure 5a–g show a comparison of the physical magnitudes that can be measured in SANS and MD experiments illustrating with examples of our data in $Bi_2Sr_2CaCu_2O_{8+\delta}$.

Figure 6 shows the field-evolution of $I(q_{Bragg}) \times q_{Bragg}$ measured at the Bragg wave-vector $q_{Bragg} = 2\pi/a_0$ and normalized by its value at zero field for a large P sample. In the London limit when vortices are sufficiently separated (see Supplementary Note 2), this magnitude is field-independent only if S_{SANS} is constant. We also include in Fig. 6 data from (K, Ba)BiO_3 considered in the literature as decisive to confirm that the phase at $B < B_{ord-dis}$ is the Bragg glass[28]. For $B/B_{ord-dis} < 1$, data for both systems are remarkably similar: $I(q_{Bragg}) \times q_{Bragg}$ is field-independent for $B \lesssim 0.4B_{ord-dis}$ and decreases exponentially beyond $0.4B_{ord-dis}$. In the vicinity of the glass-to-glass transition, $I(q_{Bragg}) \times q_{Bragg} \sim 0.1$ for both systems. For $B \sim B_{ord-dis}$ and beyond, the reported SANS intensity in (K, Ba)BiO_3[28] is below the noise level.

In contrast, in our measurements we are able to detect a measurable intensity in the vortex glass. We have a gain of two orders of magnitude in the neutron flux with respect to previous works due to the virtuous combination of measuring a larger sample and increasing the counting time. We are able to detect a non-negligible normalized neutron intensity of 6×10^{-2} for $B > B_{ord-dis}$. We found that in the vortex glass of $Bi_2Sr_2CaCu_2O_{8+\delta}$ $I(q_{Bragg}) \times q_{Bragg}$ also continues decaying, roughly exponentially, in almost two decades more in B. For the field-range of our measurements, vortices are in the London limit approximation and $f(q_{Bragg}) \times q_{Bragg}$ is constant with field, see Supplementary Note 2[39]. The decay of $I(q_{Bragg}) \times q_{Bragg}$ then comes only from a reduction of S_{SANS}, undoubtedly implying a worsening of the structural properties of the vortex glass in $Bi_2Sr_2CaCu_2O_{8+\delta}$.

When measuring in Bragg condition, six diffraction peaks are always observed in the vortex glass phase even up to $B/B_{ord-dis} = 1.8$, but their average azimuthal width grows with field. In order to quantify the degradation of orientational order in the bulk of the structure, we measure the average azimuthal width of Bragg peaks $\sigma_\perp^2$ (in units of $Å^{-1}$) from $I(\Psi, q_{Bragg})$ profiles, see Fig. 5. Taking into account the instrumental resolution, we estimate the in-plane azimuthal correlation length, $\xi_\perp = 1/(\sqrt{\sigma_\perp^2 - \sigma_{\perp inst}^2})$, the typical scale at which the shear-induced displacement of vortices in the bulk is $\sim a_0$[50]. The normalized $\xi_\perp/a_0$ obtained from SANS in sample P decreases with field in the Bragg glass up to $B/B_{ord-dis} \sim 0.6$, remains constant or slightly recovers (difficult to ascertain within the experimental error) up to $B_{ord-dis}$, and finally decreases with field in the vortex glass, see Fig. 7. This azimuthal widening of the Bragg peaks in the vortex glass is in agreement with the MD evidence on the fracturing into large crystallites with non-hexatic orientational order inside them.

In order to quantitatively support this agreement, MD data can be analyzed in a similar fashion as to obtain the in-plane azimuthal correlation length at the sample surface. The results after analyzing the azimuthal width of the peaks in $S_{MD}(q,\Psi)$ are shown with full circles in Fig. 7. Turning on field from zero to $B/B_{ord-dis} \sim 0.1$, $\xi_\perp/a_0$ enhances for both pristine and electron-irradiated samples. For this field range not covered by our SANS experiments, the vortex polycrystal observed by MD presents larger crystallites on increasing B. For the range of fields were MD and SANS data are both available, the ξ_{perp}/a_0 obtained in MD experiments decreases and seems to stagnate with B within the Bragg glass. In the vortex glass, $\xi_\perp/a_0$ is slightly smaller than in the Bragg glass. The value of this correlation length obtained from

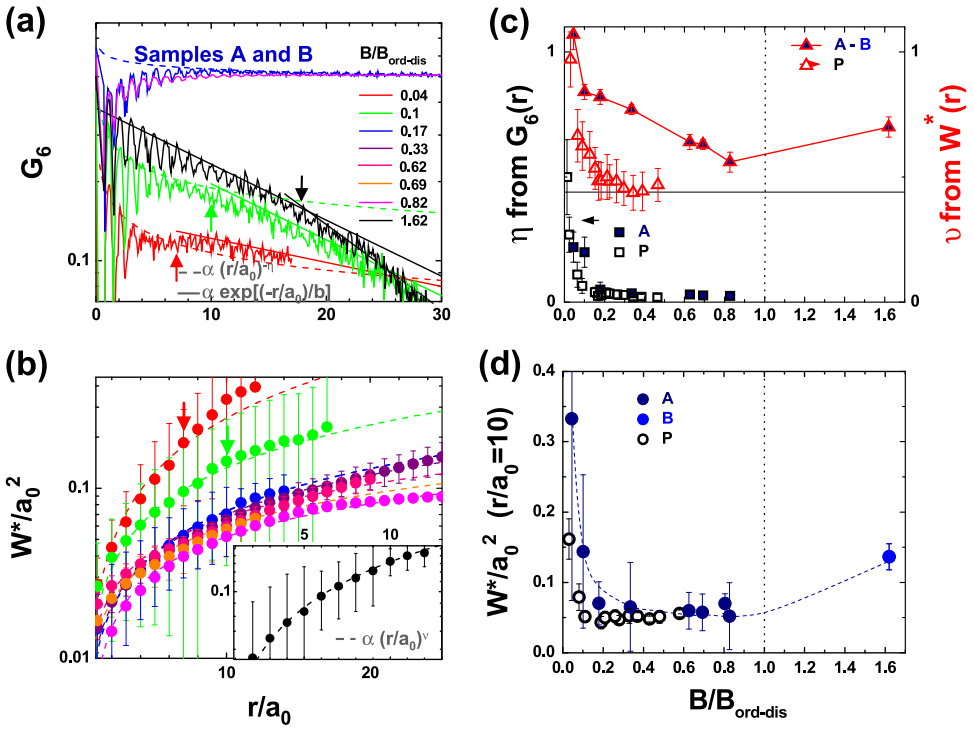

Fig. 4 Orientational and positional order of the vortex and Bragg glass phases of $Bi_2Sr_2CaCu_2O_{8+\delta}$ vortex matter at the surface of electron-irradiated samples A and B. Data obtained from magnetic decoration experiments. **a** Orientational correlation function G_6 for various normalized fields $B/B_{\mathrm{ord-dis}}$, with $B_{\mathrm{ord-dis}}$ the order–disorder transition field. Arrows indicate the size of crystallites. **b** Displacement correlator W^*/a_0^2 calculated using the lanes algorithm avoiding the effect of topological defects. Data shown following the same color-code as in **a**. Insert: detail of the fit for data obtained at $B/B_{\mathrm{ord-dis}} = 1.62$. Dashed lines correspond to fits with an algebraic decay whereas full lines are exponential fits. **c** Exponents from the algebraic fittings of $G_6(r)$ (left axis, squares) and of $W^*(r)/a_0^2$ (right axis, triangles) for the Bragg and vortex glass phases of pristine P and electron-irradiated A and B samples. The dashed red line indicates the characteristic value of $\nu = 0.44$ expected for the random manifold regime. **d** Field-evolution of the displacement correlator at a fixed lattice spacing, $W^*(r/a_0 = 10)/a_0^2$. In all panels error bars correspond to the standard error of the mean

MD experiments is larger than from SANS, and therefore the described evolution is pictorially less evident in a semi-log plot as that of Fig. 7. This difference comes from the inequality between the S_{MD} and S_{SANS}, the latter integrating the meandering of vortices along the sample thickness, the former having information from the location of vortices at the surface only. In addition, the SANS signal is collected in a sample one order of magnitude larger than those studied by MD, and then the cumulative effect of topological defects on decreasing the correlation lengths is strongest. Independently of these technical details, our MD and SANS data provide novel evidence that in the vortex glass, the structure fractures into large non-hexatic domains in the plane, at odds with some previous theoretical proposals [35].

Shortening of the positional order in the vortex glass. Further characterization of the structural changes entailed at the glass-to-glass vortex transition is get by quantifying the positional order and the radial in-plane and longitudinal correlation lengths at the bulk of the sample. Theoretically, elastic approaches showed that even though a weak random disorder destroys the perfectly hexagonal structure, quasi long-range positional order and algebraically divergent peaks in the structure factor are expected in the Bragg glass phase[27]. Previous measurements for pristine samples show resolution-limited fine Bragg peaks[39], and a distance-evolution of the positional correlation function[43] and displacement correlator[51] at the surface consistent with the random manifold regime of the Bragg glass. In this section we focus on the positional order characteristic of the vortex glass phase hinging our analysis on physical magnitudes used to fingerprint the Bragg glass.

One relevant magnitude to describe the positional order is the displacement correlator, $W(r) = \langle [u(r) - u(0)]^2 \rangle / 2$ with $u(r)$ the displacement of vortices from the sites of a perfect lattice, with average taken over quenched disorder and thermal fluctuations. Computing $W(r)$ for structures with topological defects as observed experimentally in MD images is not straightforward. Following a previous work by some of us[52], we tackled this problem by locally calculating $W(r)$ in structures with defects: $u(r)$ is computed from the comparison with regional perfect lattices with lanes oriented in the principal directions of the local experimental structure. The regional lanes stop running two a_0 away of any topological defect and new lanes are defined if the structure changes orientation. Using this regional algorithm we obtain a modified average displacement correlator $W^*(r)$ (see Supplementary Note 3).

Figure 4b presents the distance-evolution of W^*/a_0^2 for various fields on traversing the order–disorder transition for electron irradiated samples A and B. In the Bragg glass phase, $W^*/a_0^2 \propto (r/a_0)^{\nu}$ for electron irradiated as well as pristine samples (see Supplementary Note 4 for P samples). The exponent ν for both sets of samples decays with $B/B_{\mathrm{ord-dis}}$ in the Bragg glass phase, see Fig. 4c. For P samples ν stagnates around 0.44 for $B/B_{\mathrm{ord-dis}} > 0.2$. The algebraic decay of W^*/a_0^2 and this value of ν are expected for the random-manifold regime of the Bragg glass[53]. Even for the polycrystalline vortex structures observed at $B/B_{\mathrm{ord-dis}} \leq 0.1$, the growth of W^*/a_0^2 follows the same functionality inside the crystallites. For electron irradiated

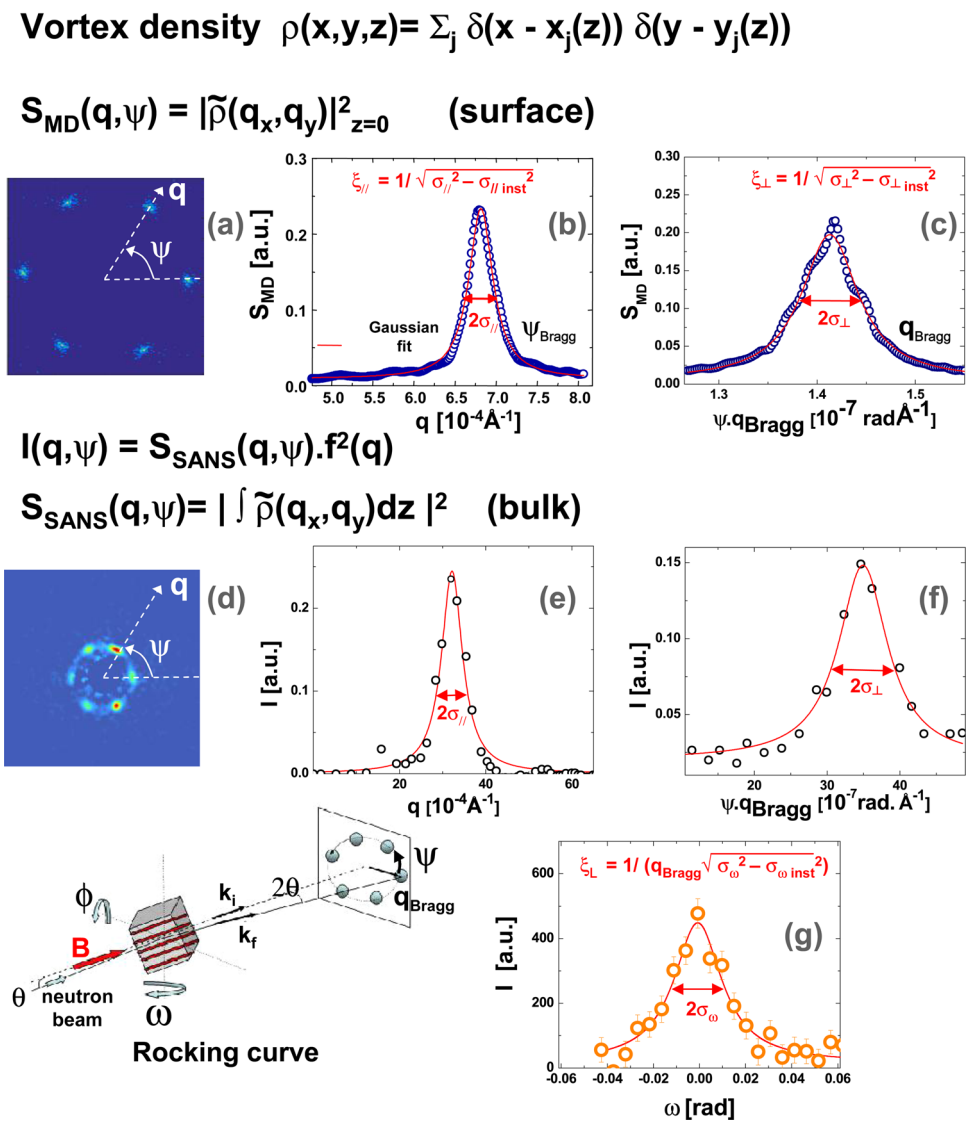

Fig. 5 In-plane and along vortices correlation lengths as measured by small-angle neutron scattering (SANS) and magnetic decoration (MD) techniques. **a** Structure factor at the sample surface obtained by imaging vortex positions with MD, $S_{MD}(q,\Psi)$. **b** Radial q-profile of S_{MD} at a fixed Ψ on traversing a Bragg peak. The figure indicates how the in-plane correlation length along the q direction, $\xi_{\parallel}/a_0$, is obtained for every Ψ considered. **c** Azimuthal Ψ-profile of S_{MD} at q_{Bragg} and estimation of the perpendicular in-plane correlation length $\xi_{\perp}/a_0$ for every q-profile considered. **d** Neutron diffraction pattern at Bragg condition proportional to the structure and the magnetic form factors of the vortex lattice $I(q,\Psi) = S_{SANS}(q,\Psi).f^2(q)$ at the whole volume of the sample. **e** Radial q-profile of $I(q,\Psi)$ on traversing a Bragg peak. **f** Azimuthal Ψ-profile of $I(q,\Psi)$. Similarly as in the case of MD, fitting each profile with Gaussians yields the two in-plane correlation lengths $\xi_{\parallel}/a_0$ and $\xi_{\perp}/a_0$. **g** Experimental configuration and typical rocking-curve data from which the longitudinal correlation length, ξ_L/a_0, can be extracted (error bars correspond to the standard error of the mean). Data correspond to pristine sample P at normalized fields $B/B_{ord-dis} = 0.15$ (**a**–**c**) and 1.25 (**d**–**g**) with $B_{ord-dis}$ the order–disorder transition field

samples, ν does not seem to stagnate for the studied fields, but reaches a value of ~ 0.5 for $B/B_{ord-dis} = 0.75$. These values of ν for the Bragg glass are one order of magnitude larger than those found for the decay of orientational order, η, indicating bond orientational order in the Bragg glass is of longer range than translational order.

In the vortex glass phase, the growth of W^*/a_0^2 can still be fitted with an algebraic growth, but the observed exponent $\nu = 0.7$ is significantly larger than in the Bragg glass. This behavior is found already at distances smaller than the typical crystallite size in the vortex glass, see data in the insert to Fig. 4b for $B/B_{ord-dis} = 1.62$. In addition, also the magnitude of the cumulated displacements at a fixed distance changes on traversing the order–disorder transition. Figure 4d shows the evolution of W^*/a_0^2 at $r/a_0 = 10$ with field: in the Bragg glass decreases up to $B/B_{ord-dis} = 0.2$, roughly stagnates up to the order–disorder transition, and has a significantly larger value in the vortex glass. Therefore, the vortex glass presents short-range positional order with $u(r)$ growing faster than in the Bragg glass.

We also quantified the positional order of the vortex glass by studying the correlation lengths in the bulk from SANS data. The radial in-plane correlation length $\xi_{\parallel}$, associated with compressive displacements of the structure, is estimated from the radial width of the Bragg peaks minus the instrumental resolution, namely $\xi_{\parallel} = 1/\sqrt{\sigma_{\parallel}^2 - \sigma_{\parallel inst}^2}$, see Fig. 5. The average q-width of the Bragg peaks, $\sigma_{\parallel}$, is slightly larger than the experimental resolution in the Bragg glass, but for $B > B_{ord-dis}$ dramatically increases with field far beyond the instrumental resolution, see Fig. 6. First, this implies that diffraction peaks in the vortex glass are not

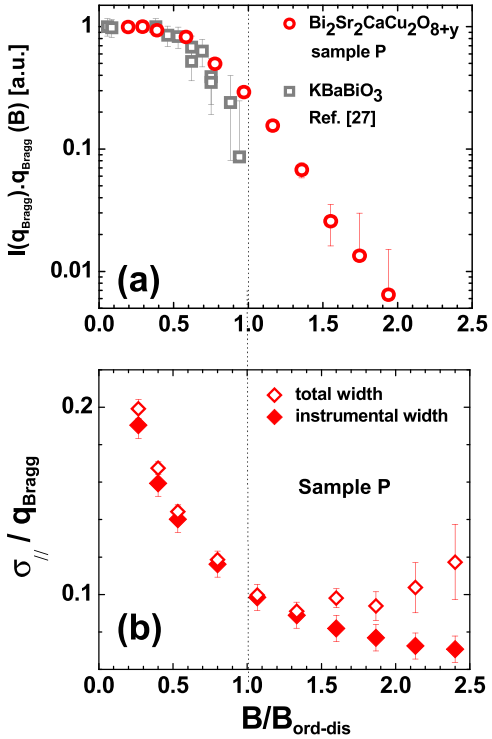

Fig. 6 Neutron diffracted intensity (at $q = q_{\mathrm{Bragg}}$) and width of the Bragg peaks as a function of the normalized field $B/B_{\mathrm{ord-dis}}$, with $B_{\mathrm{ord-dis}}$ the order-disorder transition field. **a** Normalized intensity in pristine $Bi_2Sr_2CaCu_2O_{8+\delta}$ (circles) compared to similar data in (K,Ba)BiO_3 (squares) taken from ref. [28]. Similarly as in our case, Klein et al.[28] considered $B_{\mathrm{ord-dis}} = B_{\mathrm{ON}}$, the onset field of the second-peak effect measured in (K, Ba)BiO_3. **b** Average q-width of the Bragg peaks, $\sigma_{\parallel}/q_{\mathrm{Bragg}}$, for pristine $Bi_2Sr_2CaCu_2O_{8+\delta}$ in comparison to our instrumental resolution. Error bars correspond to the standard error of the mean

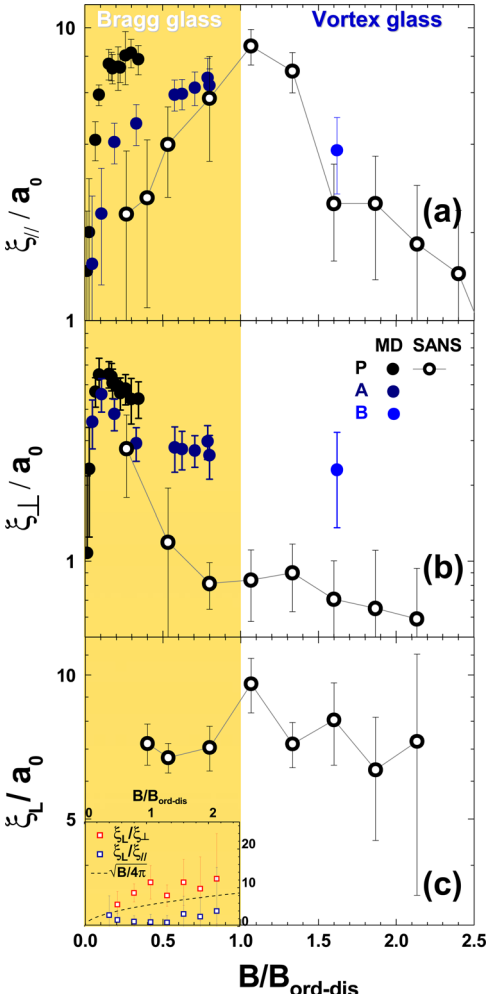

Fig. 7 Field-evolution of the in-plane and longitudinal correlation lengths obtained from magnetic decoration (MD) data collected at the surface and small-angle-neutron-scattering (SANS) data probing vortex displacements along the sample thickness. Data for the Bragg and vortex glass phases in pristine samples P and electron-irradiated samples A and B, and field normalized by the order-disorder transition field $B_{\mathrm{ord-dis}}$ for every sample. In-plane correlation lengths **a** parallel to the q-direction $\xi_{\parallel}/a_0$ and **b** along the azimuthal direction $\xi_{\perp}/a_0$. **c** Longitudinal correlation length sensitive to the meandering of vortices along the field direction. Insert: Ratio between the longitudinal and in-plane correlation lengths obtained from SANS and comparison with the field-evolution of the bending energy term, $\sqrt{c_{44}/c_{66}} \sim \sqrt{B/4\pi}$, expected for $Bi_2Sr_2CaCu_2O_{8+\delta}$ (dashed line). Error bars correspond to the standard error of the mean

resolution-limited as in the Bragg glass, but widen beyond resolution. Second, this widening yields a systematic reduction of $\xi_{\parallel}$ with field, even in units of a_0, see Fig. 7. This data for sample P obtained with SANS are consistent with the reduction of $\xi_{\parallel}$ observed with MD at the surface of pristine and electron-irradiated samples. Similarly as in the case of $\xi_{\perp}$, MD are generally above SANS data since the latter convolute information from the sample volume (see Supplementary Note 5).

We get extra information on the structural properties along the direction of vortices by measuring SANS rocking curves tilting the sample around the ω direction in the Bragg condition, see Fig. 5. The width of the rocking curve, once corrected by the instrumental resolution, gives the longitudinal correlation length associated with tilting displacements, $\xi_{\mathrm{L}} = 1/\sqrt{\sigma_{\omega}^2 - \sigma_{\omega\ inst}^2}$. This characteristic length is a measure of the spontaneous vortex meandering along the magnetic induction direction, indicating at which thickness longitudinal displacements become $\sim a_0$. Previous results in (K,Ba)BiO_3 indicated that in the Bragg glass phase the width of the rocking curve is constant and resolution-limited within an experimental resolution of $\Delta\omega \sim 0.18°$ (ref. [28]).

In our measurements in $Bi_2Sr_2CaCu_2O_{8+\delta}$ with a resolution $\Delta\omega \sim 0.1°$, the corrected width of the rocking curve is not changing appreciably in the Bragg glass up to $B/B_{\mathrm{ord-dis}} \sim 0.6$. However, at $B/B_{\mathrm{ord-dis}} \sim 0.8$, the rocking curve shrinks and ξ_{L}/a_0 increases around 30%. On entering the vortex glass, the longitudinal correlation length seems to smoothly decrease, although error bars are quite large since the diffracted intensity decreases exponentially with field. Nevertheless, we have sufficient instrumental resolution as to ascertain that no dramatic collapse of ξ_{L}/a_0 is observed in the vortex glass. The shortening of the positional order in the vortex glass is then more dramatic for in-plane than for longitudinal displacements.

In an elastic description of the vortex lattice, the ratio between the longitudinal and in-plane correlation lengths are proportional to the tilting energy, namely $\xi_{\mathrm{L}}/\xi_{\perp,\parallel} \sim \sqrt{c_{44}/c_{66}}$[14]. To evaluate this ratio in the case of $Bi_2Sr_2CaCu_2O_{8+\delta}$ with $\lambda = 2\times10^{-5}$ cm, we first consider that $c_{44} = B^2/4\pi(1+\lambda^2k^2) \approx B^2/4\pi$ since we are taking into account elastic distortions with $k \sim 1/\xi_L \sim 10^{-4}$ cm, and then $\lambda^2k^2 \sim 10^{-2} \ll 1$. The shear elastic constant is then $c_{66} \approx \Phi_0 B/(8\pi\lambda)^2 \sim B$, given the λ value for this material and $\Phi_0 = 2.07\times10^{-7}$ G.cm^2. These considerations yield $\sqrt{c_{44}/c_{66}} \simeq$

$\sqrt{B/4\pi}$ in an elastic description for $Bi_2Sr_2CaCu_2O_{8+\delta}$. The insert to Fig. 7 shows the field-evolution of the longitudinal (and radial) to azimuthal correlation lengths measured by SANS. These ratios are very close to $\simeq \sqrt{B/4\pi}$, suggesting that the eventual density of screw dislocations is not as large as to plastic deformations along the direction of vortices being dominant in the vortex glass. In summary, our in-plane MD and bulk SANS data reveal that the positional order of the vortex glass is characterized by displacements algebraically growing with distance within crystallites and that entanglement along the vortex direction seems to be unlikely. Therefore, our results are not only against the vortex glass being an amorphous phase in the plane, but also are at odds with the theoretical proposal of an in-plane disordered and out-of-plane entangled system.

Discussion

The overall decrease of the two in-plane correlation lengths on transiting into the vortex glass, detected via MD and SANS, is accompanied by a reduction of $I(q_{\rm Bragg}) \times q_{\rm Bragg}$. This intensity starts falling down for $B/B_{\rm ord-dis} \sim 0.4$ and close to the order–disorder transition decreases by one order of magnitude. This quantitative evolution was also measured in other compounds[28,40], but for our SANS experiments in $Bi_2Sr_2CaCu_2O_{8+\delta}$ we still have a significant signal in the vortex glass, and in our case this steep decrease is due to a falling down of the structure factor $S_{SANS}(q,\Psi)$ since the form factor is field-independent for our field range. The concomitant widening of the Bragg peaks, and the collapse of diffracted intensity measured by SANS in the bulk, are consistent with the non-hexatic vortex glass fracturing into large crystallites with a shortening of positional order at the surface as revealed by MD. These results in $Bi_2Sr_2CaCu_2O_{8+\delta}$ are consistent with recent SANS data in pnictide superconductors[40]. Therefore, in this particular order–disorder transition no two-stage structural transformation is detected.

The vortex system in this extremely layered superconductor undergoes a first-order glass-to-glass transition between a quasi-crystalline Bragg glass to a non-hexatic and short-range positionally ordered vortex glass with no dramatic loss of correlation along the direction of vortices. Strikingly, we obtain our results in an extremely layered type-II superconductor with flux lines formed by columns of two-dimensional pancake vortices that are longitudinally weakly-bounded, specially at high temperatures. The slight decay of ξ_L/a_0 that remains finite for $B/B_{\rm ord-dis} > 1$ suggests that in the vortex glass phase of $Bi_2Sr_2CaCu_2O_{8+\delta}$ the flux lines are formed by pancake vortices still well coupled along the c-axis direction. This might be at the origin of the glass-to-glass transition in $Bi_2Sr_2CaCu_2O_{8+\delta}$ not being well described by the two-stage melting theory for two dimensions[8]. Therefore, our results reminds that ubiquitous order–disorder transitions in nature, either melting or glass-to-glass, are strongly influenced by the dimensionality of the system, in the case of vortex matter controlled by the electronic anisotropy of the host superconductor.

Our results are a comprehensive study of the structural properties at the surface and volume of the glassy phases of vortex matter, and shed light on the structural changes undergone in defect-mediated structural transitions in general. By applying MD and SANS we are able to complement information on the in-plane correlation functions with a quantification of the typical lengths associated to the meandering of vortices in the longitudinal direction. In particular, for the case of an extremely layered type-II superconductor, we found that in the disordered glassy phase, intermediate to the quasi-crystalline and strongly entangled liquid phases, vortices are neither decoupled nor even strongly entangled along the longitudinal direction. In this phase the structure fractures into large non-hexatic domains with algebraically growing in-plane displacements. Therefore, our work reveals that for defect-driven structural transitions in systems of elastic lines, disorder does not always produce entanglement of lines. These findings enrich the possibilities of the different glassy phases in which soft condensed matter can nucleate upon introducing point disorder.

Methods

Sample preparation. We studied electron-irradiated as well as pristine $Bi_2Sr_2CaCu_2O_{8+\delta}$ samples from different sample growers. The pristine optimally doped sample used in SANS experiments is a large single crystal of $30\times5\times1.2$ mm^3 grown at the International Superconductivity Technology Center of Tokyo, Japan, by A. Rykov, and characterized at Ensicaen, France. A small part of this sample was cut for MD studies performed also in others $\sim$ 30 small single crystals grown, annealed and characterized at both, the Low Temperature Lab of Bariloche, Argentina[44], and the Kamerlingh Onnes Lab at Leiden, The Netherlands. The slightly-overdoped electron-irradiated samples (grown in a 200 mbar O_2 atmosphere at Leiden) were irradiated with 2.3 MeV electrons at low temperatures (20 K) in a van de Graaff accelerator coupled to a closed-cycle hydrogen liquifier at the École Polytechnique of Palaiseau, France[42]. Two single crystals with a significant decrease of the $B_{\rm ord-dis}$ order–disorder transition field were selected for the MD study. Sample A was annealed at 793 °C in air and then irradiated with a dose of 1.7×10^{19} e/cm^2; sample B was not annealed and irradiated with 7.4×10^{19} e/cm^2. Electrons traverse the whole sample thickness generating a roughly homogeneous distribution of point defects in the crystal structure. Irradiating at temperatures lower than the threshold temperature for defect migration is essential in order to prevent the agglomeration of defects. Some of the point defects annihilate on warming the samples, but the remaining defects are of atomic size [42].

Local Hall magnetometry. We applied local Hall probe magnetometry in order to track the changes produced in the vortex phase diagram by the point-defect potential introduced by electron irradiation. The local stray field of the samples is measured with an array of GaAs/AlGaAs Hall probes with active areas of 16×16 μm^2 (ref. [54]). We performed dc and ac measurements applying constant, H, and ripple, h_{ac}, fields parallel to the c-axis of the samples. Measuring the sample magnetization, $H_s = B - H$, when cycling H at fixed temperatures allow us to obtain dc magnetic hysteresis loops as shown in see Supplementary Fig. 1a. The separation between the ascending and descending branches of the dc loops is proportional to the critical current and develops a peak in the vicinity of the order–disorder transition, see Supplementary Fig. 1b. ac transmittivity measurements are performed by simultaneously acquiring the first and third harmonics of the ac magnetic induction when applying a ripple h_{ac} field either by changing temperature at fixed H or cycling H at fixed temperature. The transmittivity T' is obtained by normalizing the in-phase component of the first-harmonic signal B', namely $T' = [B'(T) - B'(T \ll T_c)]/[B'(T > T_c) - B'(T \ll T_c)]$, see Supplementary Fig. 1c[55]. This magnitude is extremely sensitive to discontinuities in the local induction as the B-jump produced at the first-order vortex transition at $B_{\rm FOT}$. The third harmonic signal, $|T_{h3}| = |B^{AC}_{h3}|/[B'(T > T_c) - B'(T \ll T_c)]$, is measured to detect the onset of non-linearities in the magnetic response, see Supplementary Fig. 1d. ac measurements were typically performed with ripple fields of 1 Oe amplitude and 7.1 Hz frequency. Further details are discussed in the Supplementary Note 1.

Magnetic decoration. In order to directly image individual vortex positions in a typical field-of-view of 1000–5000 vortices, MD experiments were performed simultaneously in electron-irradiated and pristine $Bi_2Sr_2CaCu_2O_{8+\delta}$ samples. The structural properties of vortex matter were imaged below and above the B_{SP} order–disorder transition by field-cooling the samples from room temperature down to 4.2 K at applied fields $5 < H < 150$ Oe. Further details in the decoration protocol followed in this case can be found in ref. [47]. Magnetic decorations were performed at different fields in roughly 30 pristine freshly cleaved small single crystals from two sample growers. For every field, experiments were performed at several realizations for statistical purposes. In the case of the two electron-irradiated samples, experiments were performed at different fields on subsequently cleaving the samples. Since this is a destructive process, every sample was first studied with Hall magnetometry and then decorated.

Small-angle neutron scattering. SANS experiments were performed at the D22 diffractometer of the Institut von Laue Langevin at Grenoble, France. The wavelength of incident neutrons was of 9 and 15 Å with a wavelength resolution of 10%. The collimation of the incident beam produced a beam divergence of $\delta(2\theta)_{div} \sim 0.1\times10^{-3}$ rad. The angular distribution of the scattered intensity, $I(q,\Psi)$, was measured in a 102.4×98 cm^2 detector with 1280×1225 pixel^2 (0.8×0.8 mm^2 per pixel) located at 17.6 m from the sample. SANS data were obtained by rocking horizontally (ϕ direction) and vertically (ω direction) the whole sample and magnet system when aligned in the Bragg condition[39]. In order

to obtain the signal coming purely from the vortex lattice, we subtracted from the raw data the normal-state background signal measured at zero field and 10 K. Similarly as in MD experiments, vortex diffraction patterns and rocking curves were measured at 4.2 K after field-cooling the sample in a magnetic field applied along the c-axis and with magnitude ranging 100 to 1000 Oe.

Data availability

All relevant data are available from the authors upon request.

Received: 3 April 2019; Accepted: 17 October 2019;
Published online: 12 November 2019

References

1. Mydosh, J. A. *Spin Glasses*. (Taylor & Francis, London, 1993).
2. Grimes, C. C. & Adams, G. Evidence for a liquid-to-crystal phase transition in a classical, two-dimensional sheet of electrons. *Phys. Rev. Lett.* **42**, 795–798 (1979).
3. Murray, C. A. & Van Winkle, D. H. Experimental observation of two-stage melting in a classical two-dimensional screened Coulomb system. *Phys. Rev. Lett.* **58**, 1200–1203 (1987).
4. Marcus, A. H. & Rice, S. A. Observations of first-order liquid-to-hexatic and hexatic-to-solid phase transitions in a confined colloid suspension. *Phys. Rev. Lett.* **77**, 2577–2580 (1996).
5. Thorneywork, A. L., Abbott, J. L., Aarts, D. G. A. L. & Dullens, R. P. A. Two-dimensional melting of colloidal hard spheres. *Phys. Rev. Lett.* **118**, 158001 (2017).
6. Thomas, H. M. & Morfill, G. E. Melting dynamics of a plasma crystal. *Nature* **379**, 806–809 (1996).
7. Deutschländer, S., Horn, T., Löwen, H., Maret, G. & Keim, P. Two-dimensional melting under quenched disorder. *Phys. Rev. Lett.* **111**, 098301 (2013).
8. Kosterlitz, J. M. & Thouless, D. J. Ordering, metastability and phase transitions in two-dimensional systems. *J. Phys. C* **6**, 1181–1203 (1973).
9. Halperin, B. I. & Nelson, D. R. Theory of two-dimensional melting. *Phys. Rev. Lett.* **41**, 121–124 (1978).
10. Nelson, D. R. & Halperin, B. I. Dislocation-mediated melting in two dimensions. *Phys. Rev. B* **19**, 2457–2484 (1979).
11. Young, A. P. Melting and the vector Coulomb gas in two dimensions. *Phys. Rev. B* **19**, 1855–1866 (1979).
12. Chui, S. T. Grain-boundary theory of melting in two dimensions. *Phys. Rev. B* **28**, 178–194 (1983).
13. Kosterlitz, J. M. The critical properties of the two-dimensional xy model. *J. Phys. C* **7**, 1046–1060 (1974).
14. Blatter, G., Feigel'man, M. V., Geshkenbein, V. B., Larkin, A. I. & Vinokur, V. M. Vortices in high-temperature superconductors. *Rev. Mod. Phys.* **66**, 1125–1388 (1994).
15. Pardo, F., de la Cruz, F., Gammel, P. L., Bucher, E. & Bishop, D. J. Observation of smectic and moving-Bragg-glass phases in flowing vortex lattices. *Nature* **396**, 348–350 (1998).
16. Troyanovski, A. M., Aarts, J. & Kes, P. H. Collective and plastic vortex motion in superconductors at high flux densities. *Nature* **399**, 665–668 (1999).
17. Menghini, M., Fasano, Y. & de la Cruz, F. Critical current and topology of the supercooled vortex state in $NbSe_2$. *Phys. Rev. B* **65**, 064510 (2002).
18. Fasano, Y. et al. Order-disorder phase transition in $NbSe_2$: absence of amorphous vortex matter. *Phys. Rev. B* **66**, 020512(R) (2002).
19. Petrović, A. P. et al. Real-space vortex glass imaging and the vortex phase diagram of $SnMo_6 S_6$. *Phys. Rev. Lett.* **103**, 257001 (2009).
20. Guillamón, I. et al. Enhancement of long-range correlations in a 2D vortex lattice by an incommensurate 1D disorder potential. *Nat. Phys.* **10**, 851–856 (2014).
21. Zehetmayer, M. How the vortex lattice of a superconductor becomes disordered: a study by scanning tunneling spectroscopy. *Sci. Rep.* **5**, 9244 (2015).
22. Ganguli, S. C. et al. Disordering of the vortex lattice through successive destruction of positional and orientational order in a weakly pinned $Co_{0.0075} NbSe_{0.0075}$ single crystal. *Sci. Rep.* **5**, 10613 (2015).
23. Toft-Petersen, R., Abrahamsen, A. B., Balog, S., Porcar, L. & Laver, M. Decomposing the Bragg glass and the peak effect in a Type-II superconductor. *Nat. Commun.* **9**, 901 (2018).
24. Shibauchi, T. et al. Interlayer phase coherence in the vortex matter phases of $Bi_2Sr_2CaCu_2O_{8+y}$. *Phys. Rev. Lett.* **83**, 1010–1013 (1999).
25. Gaifullin, M. B., Matsuda, Y., Chikumoto, N., Shimoyama, J. & Kishio, K. Abrupt change of josephson plasma frequency at the phase boundary of the bragg glass in $Bi_2 Sr_2 CaCu_2 O_2$. *Phys. Rev. Lett.* **84**, 2945–2948 (2000).
26. Nattermann, T. Scaling approach to pinning: charge-density waves and giant flux creep in superconductors. *Phys. Rev. Lett.* **64**, 2454–2457 (1990).
27. Giamarchi, T. & LeDoussal, P. Elastic theory of flux lattices in the presence ef wreak disorder. *Phys. Rev. B* **52**, 1242–1270 (1995).
28. Klein, T. et al. A Bragg glass phase in the vortex lattice of a type II superconductor. *Nature* **413**, 404–406 (2001).
29. Nattermann, T. & Scheidl, S. Vortex-glass phases in type-II superconductors. *Adv. Phys.* **49**, 607–704 (2000).
30. Avraham, N. et al. 'Inverse' melting of a vortex lattice. *Nature* **411**, 451–454 (2001).
31. Vinokur, V. M. et al. Lindemann criterion and vortex-matter phase transitions in high-temperature superconductors. *Phys. C Supercond.* **295**, 209–217 (1998).
32. Khaykovich, B. et al. Vortex-matter phase transitions in $Bi_2 Sr_2 CaCu_2 O_2$: effects of weak disorder. *Phys. Rev. B* **56**, R517–R520 (1997).
33. Cubitt, R. et al. Direct observation of magnetic flux lattice melting and decomposition in the high-Tc superconductor $Bi_{2.15} Sr_{2.15} CaCu_{2.15} O_{2.15}$. *Nature* **365**, 407–411 (1993).
34. Pastoriza, H., Goffman, M. F., Arribére, A. & de la Cruz, F. First order phase transition at the irreversibility line of $Bi_2 Sr_2 CaCu_2 O_2$. *Phys. Rev. Lett.* **72**, 2951–2954 (1994).
35. Chudnovsky, E. M. Orientational and positional order in flux lattices of type-II superconductors. *Phys. Rev. B* **43**, 7831–7836 (1991).
36. Koshelev, A. E. & Vinokur, V. M. Pinning-induced transition to disordered vortex phase in layered superconductors. *Phys. Rev. B* **57**, 8026–8033 (1998).
37. Kierfeld, J. & Vinokur, V. M. Lindemann criterion and vortex lattice phase transitions in type-II superconductors. *Phys. Rev. B* **69**, 024501 (2004).
38. Forgan, E. M., Wylie, M. T., Lloyd, S., Lee, S. L. & Cubitt, R. Observation of a re-emergence of the flux lattice in BSCCO. *Czech. J. Phys.* **46**, 1571–1572 (1996).
39. Pautrat, A. et al. Persistence of an ordered flux line lattice above the second peak in $Bi_2 Sr_2 CaCu_2 O_2$. *Phys. Rev. B* **75**, 224512 (2007).
40. Demirdiş, S., van der Beek, C. J., Mühlbauer, S., Su, Y. & Wolf, Th SANS study of vortex lattice structural transition in optimally doped $(Ba_{1-x} K_{1-x})Fe_{1-x} As_{1-x}$. *J. Phys. Condens. Matter* **28**, 425701 (2016).
41. Fasano, Y. & Menghini, M. Magnetic-decoration imaging of structural transitions induced in vortex matter. *Supercond. Sci. Technol.* **21**, 023001 (2008).
42. Konczykowski, M. et al. Vortex matter in $Bi_2 Sr_2 CaCu_2 O_2$ with pointlike disorder. *J. Phys. Conf. Ser.* **150**, 052119 (2009).
43. Fasano, Y., De Seta, M., Menghini, M., Pastoriza, H. & de la Cruz, F. Commensurability and stability in nonperiodic systems. *Proc. Natl Acad. Sci. USA* **102**, 3898–3902 (2005).
44. Correa, V. F., Kaul, E. E. & Nieva, G. Overdoping effects in $Bi_2 Sr_2 CaCu_2 O_2$: From electromagnetic to Josephson interlayer coupling. *Phys. Rev. B* **63**, 172505 (2001).
45. Pardo, F., Mackenzie, A. P., de la Cruz, F. & Guimpel, J. Effect of the reversibility region on the low-temperature vortex structure imaged by Bitter magnetic decoration. *Phys. Rev. B* **55**, 14610–14613 (1997).
46. CejasBolecek, N. R. et al. Vortex matter freezing in $Bi_2 Sr_2 CaCu_2 O_2$ samples with a very dense distribution of columnar defects. *Phys. Rev. B* **93**, 054505 (2016).
47. Fasano, Y., Herbsommer, J. A. & de la Cruz, F. Superficial periodic pinning induced by Bitter decoration applied to the study of vortex structure nucleation and growth. *Phys. Stat. Sol. B* **215**, 563–571 (1999).
48. Wördenweber, R. & Kes, P. H. Dimensional crossover in collective flux pinning. *Phys. Rev. B* **34**, 494–497 (1986).
49. Menon, G. I. Phase behavior of type-II superconductors with quenched point pinning disorder: a phenomenological proposal. *Phys. Rev. B* **65**, 104527 (2002).
50. Gammel, P. L. et al. Structure and correlations of the flux line lattice in crystalline Nb through the peak effect. *Phys. Rev. Lett.* **80**, 833–8367 (1998).
51. Kim, P., Yao, Z., Bolle, C. A. & Lieber, C. M. Structure of flux line lattices with weak disorder at large length scales. *Phys. Rev. B* **60**, R12589–R12592 (1999).
52. CejasBolecek, N. R. et al. Excess of topological defects induced by confinement in vortex nanocrystals. *Phys. Rev. B* **96**, 024507 (2017).
53. Giamarchi T. & Bhattacharya S. *Vortex Phases in "High Magnetic Fields: Applications in Condensed Matter Physics and Spectroscopy"* (eds Berthier C et al.) Vol. 9, p. 314. (Springer-Verlag, New York, 2002).
54. Dolz, M. I. et al. Latent heat and nonlinear vortex liquid in the vicinity of the first-order phase transition in layered high-T_c superconductors. *Phys. Rev. B* **90**, 144507 (2014).
55. Gilchrist, J. & Konczykowski, M. Superconductor screen viewed as one or two inductive loops. *Phys. C Supercond.* **212**, 43–60 (1993).

Acknowledgements

This work was supported by the ECOS-Sud-MINCyt France-Argentina bilateral program under Grant A09E03; by the Argentinean National Science Foundation (ANPCyT) under

Grants PRH-PICT 2008-294 and PICT 2011-1537; by the Universidad Nacional de Cuyo research grants program; and by Graduate Research fellowships from IB-CNEA for J.A.S. and from CONICET for R.C.M., G.R., and N.R.C.B. We thank to M. Li and A. Rykov for growing some of the studied pristine single crystals and V. Moser for providing us the Hall sensors.

Author contributions

Y.F., A.P., M.K. and C.J.vdB. designed research; J.A.S., R.C.M., N.R.C.B., G.R., P.P., M.I.D., Ch.D.D., R.C, A.P. and Y.F. performed measurements, G.N. grow some pristine samples, M.K., and C.J.vdB. irradiated samples, A.B.K. performed theoretical research; J.A.S., Y.F. and A.P. analyzed data; Y.F. and A.B.K. wrote the paper.

Competing interests

The authors declare no competing interests.

Additional information

Supplementary information is available for this paper at https://doi.org/10.1038/s42005-019-0243-4.

Correspondence and requests for materials should be addressed to Y.F.

Reprints and permission information is available at http://www.nature.com/reprints

Publisher's note Springer Nature remains neutral with regard to jurisdictional claims in published maps and institutional affiliations.